

Harnessing plasmon-exciton energy exchange for flexible organic solar cells with efficiency of 19.5%

Received: 16 December 2024

Accepted: 16 April 2025

Published online: 23 April 2025



Jing-De Chen^{1,2}, Hao Ren^{1,2}, Feng-Ming Xie², Jia-Liang Zhang², Hao-Ze Li³, Abdul Sameeu Ibupoto², Ye-Fang Zhang², Yan-Qing Li³✉ & Jian-Xin Tang^{1,2}✉

The plasmonic effects have unlocked remarkable advancements in modern optoelectronics, enabling enhanced light-matter interactions for applications ranging from sensing to photovoltaics. However, the nonradiative damping of plasmonic effects causes parasitic absorption which limits the light-utilization efficiency of optoelectronics, particularly for photovoltaic cells. Herein, we propose a plasmon energy recycling scheme consisting of green fluorophore (BCzBN) and nickel oxide to compensate for the plasmon energy loss. The plasmons trapped in silver nanowire (AgNW) electrodes are coupled to green emission through plasmon-exciton energy exchange. Backward electron and energy transfer are inhibited due to the spectral mismatch and energy level offset. The optically enhanced flexible AgNW electrode exhibits an improvement of 10.74% in transmittance, yielding flexible organic solar cells with an efficiency of 19.51% and a certified value of 18.69%. This innovative strategy provides a pathway for overcoming plasmon energy losses in plasmonic optoelectronics, opening horizons for highly efficient flexible photovoltaics and plasmonic devices.

Plasmonic effects, arising from the collective oscillation of free electrons at the surface of metals under electromagnetic excitation, have revolutionized multiple fields of science and technology. These effects, which are particularly pronounced in nanoscale metallic structures, enable the manipulation of light at scales far smaller than the diffraction limit, leading to unprecedented advancements in optical manipulation^{1–4}. In the past decades, plasmonic nanostructures have shown transformative potential in energy conversion, playing a critical role in applications such as plasmon-enhanced photovoltaics and photocatalysis^{5–9}.

While plasmonic effects enable extraordinary control over light-matter interactions, energy loss remains a critical challenge that impacts the efficiency of energy conversion^{10–13}. Energy losses in plasmonic systems primarily arise from intrinsic material absorption

and nonradiative damping of plasmons, which limit the conversion of plasmonic excitations into useful optical or electrical energy^{14–17}. In plasmon-enhanced photovoltaics, these losses reduce the efficiency of light harvesting and the generation of charge carriers, constraining the overall device performance. Addressing these losses is essential for optimizing plasmonic nanostructures, whether through the development of low-loss materials, such as doped semiconductors, or innovative designs like hybrid plasmonic systems that couple metallic components with dielectrics or 2D materials^{12,13,18–20}.

Silver nanowire (AgNW) is a kind of widely used plasmonic structure due to its antenna and Purcell effects. It also merges as a promising component of flexible transparent electrodes (FTEs) in the field of flexible optoelectronics^{21–23}. Owing to the advances in morphology control, the properties of AgNW-based FTEs, particularly their

¹Macao Institute of Materials Science and Engineering (MIMSE), Faculty of Innovation Engineering, Macau University of Science and Technology, Taipa, Macau SAR 999078, China. ²Institute of Functional Nano & Soft Materials (FUNSOM), Soochow University, Suzhou, Jiangsu 215123, China. ³School of Physics and Electronic Science, East China Normal University, Shanghai 200241, China. ✉ e-mail: yqli@phy.ecnu.edu.cn; jxtang@must.edu.mo

transmittance and sheet resistance, now approaching those of rigid indium tin oxide (ITO) electrodes^{24–27}. Nevertheless, the efficiency of AgNW-based flexible organic solar cells (FOSCs), as reported, is still lower than that of rigid counterparts, implying a considerable energy loss in AgNW-FTEs^{28–33}. Importantly, AgNWs support localized surface plasmon resonance (LSPR) that causes energy losses in FOSCs and has not been fully understood^{14,34–36}.

In this work, we propose a plasmon energy recycling strategy to compensate for the optical loss of FOSCs. The green fluorescent material (BCzBN) doped in nickel oxide (NiO_x) hole transport layer couples LSPR to green emission through plasmon-induced resonance energy transfer (PIRET). With a rationally designed energy level structure, excited electrons are trapped in BCzBN and mostly contribute to radiative recombination. The backward electron and energy transfer are simultaneously blocked. The boosted resonance energy transfer improves the transmittance of FTE by 10.74% in the spectral region associated with LSPR. With reduced energy loss, FOSCs with a photoactive layer of D18:L8-BO obtained a state-of-the-art PCE of 19.51% and a certified PCE of 18.69%.

Results

Optical loss of AgNW-FTEs

We first examined the optical properties of AgNWs via theoretical analysis to understand the energy losses. Given the near-circular cross-section of AgNWs, Mie theory was first employed for calculation³⁷. Referring to the commonly used size of AgNWs, the diameter of the Ag nanoparticle was set to 30 nm in the calculation. Taking into consideration the potential influence of the surrounding medium on the optical dynamics of Ag nanoparticles, we adjusted the refractive index of the medium (n_{medium}) to 1.0 and 1.7, representative of air and

commonly used charge transport layers, respectively. Figure 1a displays the derived extinction efficiency (Q_{ext}), scattering efficiency (Q_{sca}), and absorption efficiency (Q_{abs}). The results suggest that absorption is the main contributor to the light extinction of Ag nanoparticles. As the n_{medium} increases, peak Q_{sca} notably rises from 0.4 to 2.0, while Q_{abs} essentially remains constant. Consequently, Q_{ext} increases from 5.8 to 8.0 as n_{medium} surges from 1.0 to 1.7, signaling improved optical loss. Moreover, the characteristic Q_{ext} peak of LSPR shifts from 370 nm to 412 nm, inevitably generating more energy loss in the FSC since AM1.5G spectrum peaked at the visible region. Notably, although $Q_{\text{abs}}/Q_{\text{ext}}$ gradually decreased with the particle size, the absolute value of Q_{abs} experienced an increase (Supplementary Fig. 1). The simultaneous increases in Q_{abs} and Q_{sca} resulted in a substantially higher Q_{ext} for larger particles. These findings imply that simply varying the diameter of AgNWs cannot mitigate the optical loss in AgNWs.

The nearfield optical dynamics of AgNWs were investigated utilizing finite difference time domain (FDTD) simulation. A straight AgNW was illuminated by downwards polarized light. A 7 nm PVP shell was also considered in the simulations referring to related reports^{38,39}. The optical spectra in Fig. 1b substantiate that increased n_{medium} results in more potent light extinction. The wavelength of the transmission valley was shifted from 360 nm to 390 nm and the transmittance (T) decreased from 83.1% to 74.9%. This is due to escalated reflectance (R) and absorbance (A), aligning with the findings of the Mie theory calculation. A notable finding from the FDTD simulation is the broadband light extinction between 300 nm and 600 nm at n_{medium} of 1.7. For a clearer grasp of the optical loss mechanisms, Fig. 1c,d depicts cross-sectional profiles of the electric field distribution of AgNWs. In a wide spectral range, only vertically symmetric

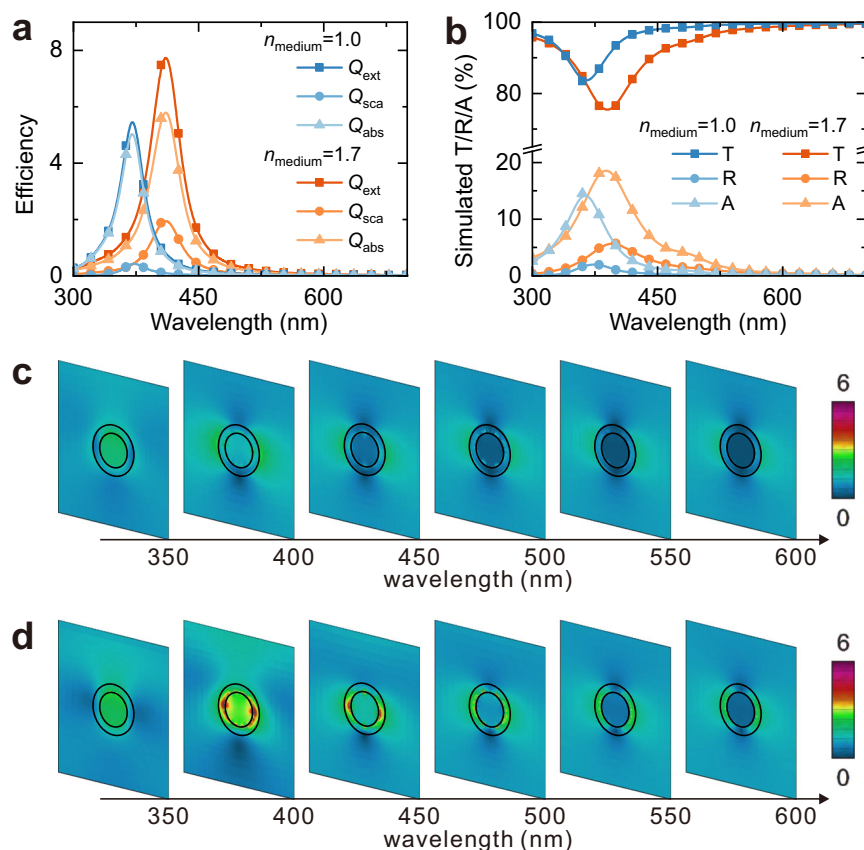


Fig. 1 | Optical energy losses analysis of AgNWs. **a** Calculated Q_{ext} , Q_{sca} , and Q_{abs} of Ag nanoparticle surrounded by media with n_{medium} of 1.0 and 1.7. **b** Simulated transmission (T), reflection (R), and absorption (A) spectra of AgNW under TM light

illumination. Wavelength-dependent simulated cross-sectional electric field distribution profiles of AgNW surrounded by medium with n_{medium} of **c** 1.0 and **d** 1.7. Source data are provided as a Source Data file.

patterns emerge, signifying the occurrence of dipolar mode LSPR^{36,40}. Due to the diameter of AgNWs being significantly smaller than the wavelength, high-order LSPRs are not supported. At n_{medium} of 1.0, the patterns faint as the wavelength exceeds 400 nm, illustrating the gradual weakening of the collective electron oscillation. In contrast, for AgNWs situated in a medium with n_{medium} of 1.7, luminescent red patterns appear at both 400 nm and 450 nm, which signify a broad spectral range of LSPR excitation in AgNWs. The full width at half maximum (FWHM) of the FDTD simulated extinction peak is 80 nm, exceeding the 41 nm from Mie theory calculation. The discrepancy may be attributed to the weaker retardation effects of LSPR in AgNW compared to Ag nanoparticles.

Plasmon energy transfer of AgNW-FTEs

There are two methods for extracting LSPR energy: one is the injection of hot electrons from the plasmonic metal structure to the neighboring semiconductor, and the other is PIRET^{41–44}. Due to inefficient hot electron injection, PIRET emerges as the sole likely mechanism for plasma energy recycling at AgNW electrodes. Therefore, a green fluorescent material (BCzBN) with a partial absorption spectrum overlapping with that of LSPR was adopted as an acceptor to trigger PIRET (Fig. 2a). Specifically, the energy of LSPR surpasses the optical

bandgap of BCzBN, making PIRET theoretically feasible⁴⁵. Any reverse energy transfer from BCzBN to AgNW, namely Förster resonance energy transfer (FRET), is limited since the emission peak of BCzBN at 510 nm doesn't coincide with the LSPR absorption peak (Fig. 2b). The excimer emission from BCzBN (around 580 nm) further retards the FRET⁴⁶. In addition, the insulating PVP shell inhibits reverse hot electron injection due to the large Schottky barrier⁴⁷. Given that the photoluminescence quantum efficiency (PLQY) of fluorescent materials approaches 100% in the doping film while much lower in neat film, a charge transport layer should be used to act as the host for doping BCzBN. The lowest unoccupied molecular orbital and highest occupied molecular orbital of BCzBN derived from the cyclic voltammetry results in Supplementary Fig. 2 are -2.9 eV and -5.4 eV, respectively. Therefore, NiO_x with a conductive band of -1.6 eV and a valance band of -5.4 eV was selected⁴⁸. Theoretically, excited electrons can be trapped in BCzBN and contribute to luminescence through radiative recombination. Simultaneously, BCzBN doesn't serve as traps for hole transportation, ensuring hole extraction is unaffected. The BCzBN-doped NiO_x used as a plasmon energy extraction layer is noted as PEEL. Figure 2b depicts the extinction spectra of AgNWs, AgNWs/ NiO_x , and AgNWs/PEEL. Echoing the simulation results, the NiO_x coating shifts the LSPR peak from 350 nm to 400 nm and broadens the extinction

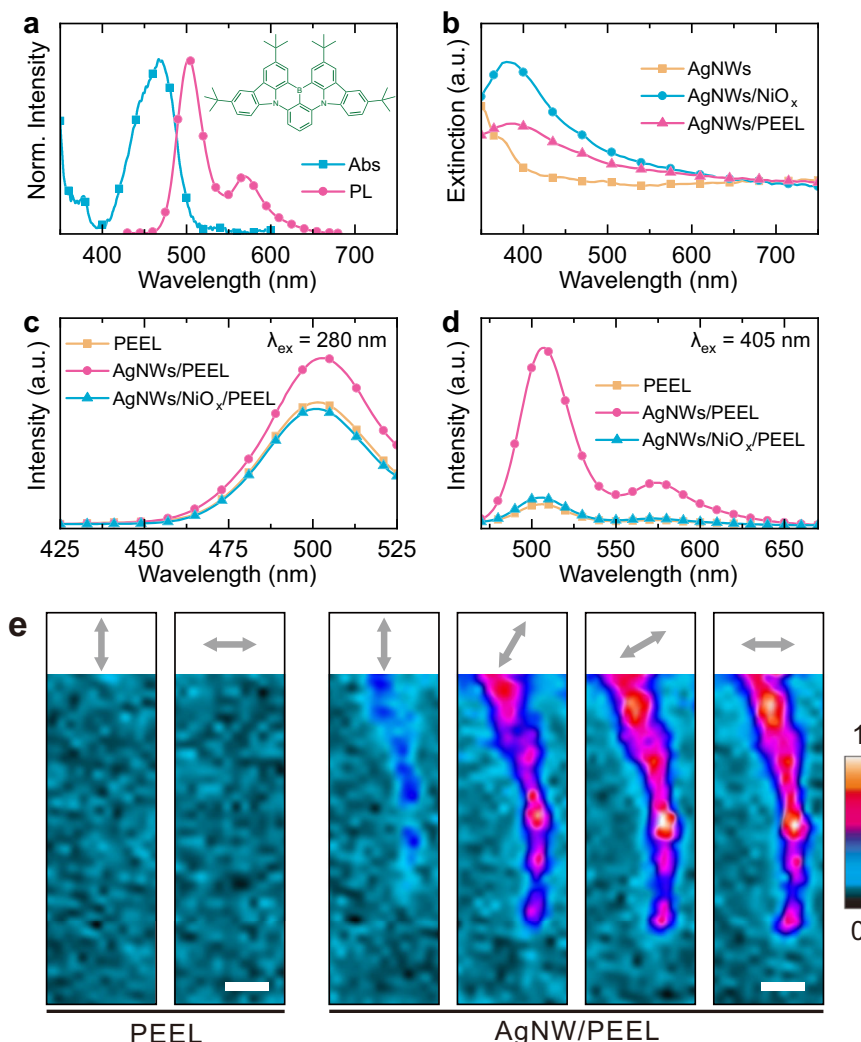


Fig. 2 | The investigation of PIRET. **a** Molecule structure, absorption spectrum, and PL spectrum of neat BCzBN film. **b** Extinction spectra of AgNWs, AgNWs/ NiO_x , and AgNWs/PEEL. PL spectra of PEEL, AgNWs/PEEL, and AgNWs/ NiO_x /PEEL under **c** 280 nm and **d** 405 nm excitation. **e** PL mapping results of PEEL and AgNW/PEEL

excited at 405 nm and recorded at 500 nm. The arrows represent the polarization direction of the light source. The scale bar is $1\ \mu\text{m}$. Source data are provided as a Source Data file.

peak. To maximize the plasmon energy recycling effect, the doping concentration of BCzBN is altered. As the extinction spectra shown in Supplementary Fig. 3, the optical loss of AgNWs/PEEL progressively decreases with increasing concentration, reaching a saturation point at 1 mg mL^{-1} . The further increase of the BCzBN doping concentration to 2.0 mg mL^{-2} increases optical loss. As revealed by Supplementary Fig. 4, large BCzBN aggregates were generated under high-concentration doping. Therefore, aggregation-induced quenching and light scattering of BCzBN were introduced simultaneously. At high doping concentrations, the decrease in photoluminescence of BCzBN emitters cannot be matched by the increase in plasmon energy recycling, resulting in higher optical losses. A doping concentration around 1.0 mg mL^{-2} balanced plasmon energy recycling and parasitic absorption of BCzBN, which results in an almost halved optical loss of AgNWs/PEEL.

The photoluminescence (PL) spectra of PEEL and AgNWs/PEEL were measured to confirm our hypothesis on plasmon energy recycling. The PL spectra detailed in Fig. 2c,d were recorded under 280 nm and 405 nm excitation, respectively. The presence of AgNWs led to a 34% enhancement in the PL intensity of PEEL under 280 nm excitation, and when the samples were subjected to 405 nm light, the enhancement ratio escalated to over 740%. Given BCzBN's weak absorption at 405 nm, the strong PL of AgNWs/PEEL is deeply linked to the LSPR of AgNWs. Referring to the extinction spectrum of AgNW/NiO_x, we assume that the PL intensity varies with the LSPR. (Fig. 2b). It is noteworthy that the enhanced PL intensity could arise from hot-electron injection, plasmon-enhanced fluorescence (PEF), and PIRET. Since AgNWs and BCzBN are separated by PVP and NiO_x, the possibility of hot electron injection in this system is minimal. In addition, the efficiency of hot electron injection is low and cannot support such significant PL enhancement. Principally, PEF enhances PL by boosting spontaneous emission from the emitter, which is more pronounced with low PLQY emitters. There is no energy exchange between plasmons and emitters, with the emitter's absorption setting the upper limit for PL intensity. The PLQY of PEEL and AgNWs/PEEL was also characterized to examine the influence of PEF on optical extinction. A light source with a wavelength of 450 nm was selected. When AgNWs were introduced, the PLQY of PEEL dropped from 93% to 75%. The near unity PLQY of PEEL suggests the low optical loss in BCzBN, even at a relatively high concentration. We could deduce that PEF might be present in AgNWs/PEEL due to the spectral overlap, but it has a limited effect on PL because of the high PLQY of BCzBN. By comparing the markedly improved PL intensity and the reduced PLQY, it can be derived that the absorbed photons in AgNWs may be partially converted to far-field radiation through PIRET between AgNWs and BCzBN.

To demonstrate the presence of PIRET, the geometrical distance between AgNWs and BCzBN was varied by inserting various numbers of neat NiO_x films since PIRET is a distance-dependent energy transfer mechanism. The PL spectra shown in Supplementary Fig. 5a indicate a gradual decrease in the PL intensity of AgNWs/PEEL with the increasing distance. Supplementary Fig. 5b relates the derived peak PL intensity to the number of NiO_x interlayers, showing an exponential decay in PL intensity which aligns with the trend of the LSPR-induced near-field enhancement. This affirms that the PL enhancement is intimately associated with PIRET. Referencing the PL spectra of AgNWs/3-NiO_x/PEEL plotted in Fig. 2c, d, three layers of NiO_x hinder energy transfer from AgNWs to BCzBN, resulting in PL intensity comparable to bare PEEL. To delve into the energy transfer mechanisms at the microscopic scale, PL mapping was also performed. Polarized light with a wavelength of 405 nm was applied. The left two images in Fig. 2e show that PEEL maintains a weak PL throughout regardless of polarization direction. This is owing to the low absorption of BCzBN at 405 nm. In contrast, the patterns of AgNWs were observed in AgNWs/PEEL (right four images of Fig. 2e). To validate LSPR energy transfer, we employed

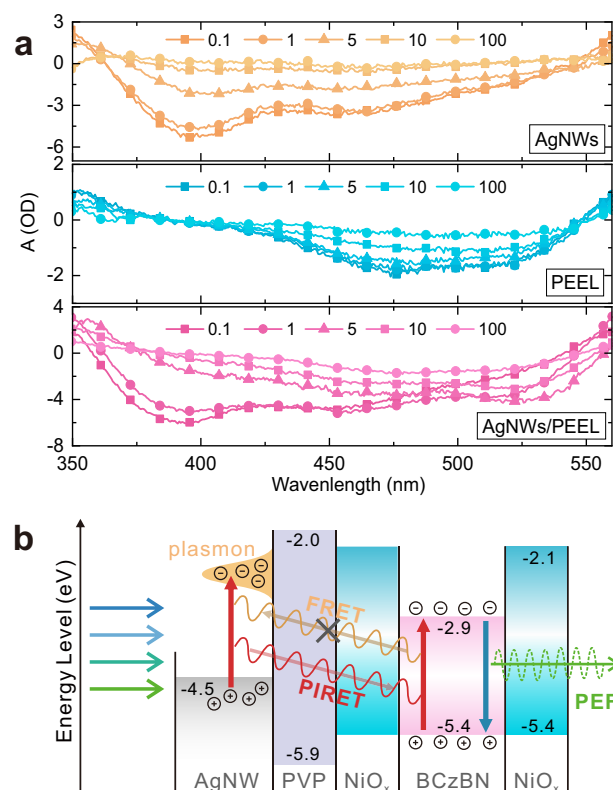


Fig. 3 | Plasmon-exciton energy exchange analysis. **a** Time-dependent TA spectra of AgNWs/NiO_x, PEEL, and AgNWs/PEEL detected at 0.1, 1, 5, 10, and 100 ps with 330 nm excitation. **b** Schematic energy level diagram of AgNWs/PEEL and energy transfer dynamics. Source data are provided as a Source Data file.

polarized light in the measurements, given that the LSPR of AgNW can only be excited by transverse magnetic (TM) light. The direction of polarization was determined from the orientation of the AgNW. The target AgNW under TM illumination showcased a pattern significantly brighter than that under transverse electric (TE) illumination. Consequently, we attribute the LSPR excitation as the source of the enhanced PL in AgNWs/PEEL. Moreover, PL mapping results reveal that lateral PIRET appreciably depends on the distance between AgNWs and BCzBN. Only the emitters proximal to AgNWs contribute to plasmon energy recycling, while others may induce parasitic absorption due to non-optimal PLQY.

Transient absorption (TA) spectra of AgNWs, PEEL, and AgNWs/PEEL were also measured to evidence the existence of PIRET. The samples were excited by 330 nm laser and their responses were recorded at delay times of 0.1, 1, 5, 10, and 100 ps. The TA spectra of AgNWs/NiO_x are depicted in Fig. 3a, corresponding to its extinction spectra, which in turn substantiates the optical loss of AgNWs/NiO_x. Due to the rapid relaxation of the LSPR, the TA signal diminishes rapidly and almost disappears at 10 ps. In contrast, the TA signal of PEEL lasts longer since the singlet excitons of BCzBN feature a lifespan extending to the nanosecond range. Notably, the expansive TA peak, sweeping from 400 to 550 nm, comprised the ground-state bleach (GSB) at 475 nm and stimulated emission (SE) at 510 nm. The vibrational relaxation of hot carriers at singlet excited states leads to the redshift of the GSB peak. The associated TA signal also exhibits a slower decay at 510 nm when compared to 475 nm. Noteworthy changes in TA spectra of AgNWs/PEEL manifest as the delay time incrementally increases. Between 0.1 and 5 ps, a decrease in the TA signal at 400 nm and a corresponding increase at 510 nm suggest effective energy transfer from AgNWs to PEEL. Similar to the PEEL, the TA signal of AgNWs/PEEL also diminishes over time. This phenomenon

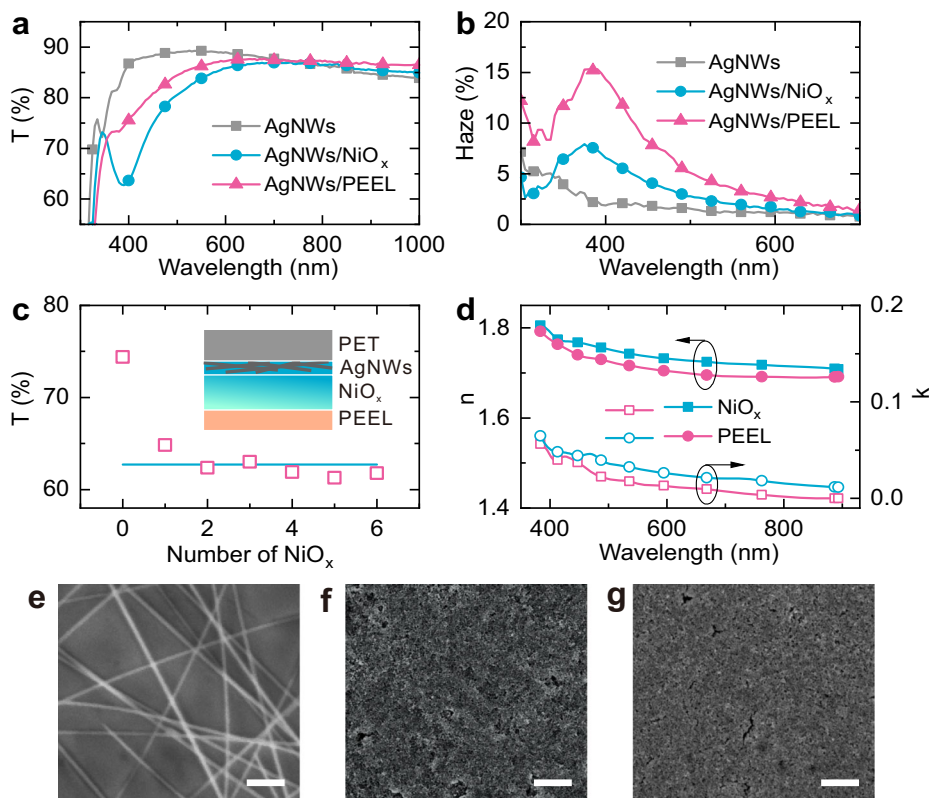


Fig. 4 | Characterization of FTEs. **a** Transmission spectra and **b** haze spectra of AgNWs, AgNWs/NiO_x, and AgNWs/PEEL. **c** Transmittance of AgNWs/PEELs with various numbers of NiO_x spacers at 400 nm. The solid line represents the

transmittance of AgNWs/NiO_x at 400 nm. **d** The refractive index of NiO_x and PEEL. SEM images of **e** AgNWs, **f** AgNWs/NiO_x, and **g** AgNWs/PEEL. The scale bar is 500 nm. Source data are provided as a Source Data file.

suggests that the excited carriers become trapped within BCzBN and undergo relaxation through radiative recombination, as pictorially demonstrated in Fig. 3b. The large Schottky barrier between BCzBN and NiO_x retards the extraction of excited electrons. Additionally, the reverse hot-electron injection from BCzBN to AgNWs is hindered by PVP. For AgNWs/PEEL illuminated by steady light, the stable LSPR may also boost spontaneous radiation of BCzBN through an intensifying near-field electric field, referring to PEF. In such circumstances, the optical loss in BCzBN is concurrently minimized. Moreover, the incessant decrease in TA signal at shorter wavelengths implies that FRET is hardly perceptible in AgNWs/PEEL. This could be attributed to the insignificant spectral overlap between the absorption of AgNWs and the emission of BCzBN.

Optical properties of AgNW-FTEs

The practical implications of PEEL were evaluated through characterizing the optical properties of AgNW FTEs. Figure 4a shows the transmission spectra of AgNWs, AgNWs/NiO_x, and AgNWs/PEEL. The AgNWs network was fabricated according to previous reports⁴⁹. Consistent with the extinction spectra, NiO_x reduces the transmittance of AgNWs in a broad spectral region from 350 to 700 nm. At 390 nm, a notable decline in transmittance is discerned as the value shifts from 84.5% to 62.7%. The incorporation of PEEL prompts a 10.7% increase in transmittance at the same wavelength, yielding an impressive transmittance of 73.4%. The inference is thus made that the PIRET recycles almost half of the LSPR energy. The decrease in transmittance of AgNWs/PEEL at around 340 nm originates from the absorption of BCzBN. The average transmittance for AgNWs, AgNWs/NiO_x, and AgNWs/PEEL in the spectral band from 350 to 1000 nm is 86.6%, 82.3%, and 84.9%, respectively. The haze spectra displayed in Fig. 4b show that bare AgNW FTE features a low haze value. Despite calculations indicating clear light scattering caused by LSPR excitation, the low-

duty cycle of AgNWs results in weak light scattering for AgNW FTE. Further, the deposition of NiO_x enhances haze, accompanied by a peak wavelength shift. These alterations are commensurate with changes in LSPR. The presence of AgNWs/PEEL corresponds to higher haze, which stems from the omnidirectional emission of BCzBN. Considering the low absorption of the advanced active layer systems in the blue region, this light scattering enhancement is beneficial for the light-harvesting capabilities of integrated devices. It is noteworthy that the sheet resistance of the bare AgNWs FTE is 9.8 Ω sq⁻¹, and it is believed that the conductivity of AgNWs remains unchanged post the preparation of the charge transporting layer.

The impact of PIRET on the transmission of AgNW FTEs was explored by altering the quantity of NiO_x optical spacers. As the transmission spectra detailed in Fig. 4c, it was observed that the transmittance of AgNWs/*m*-NiO_x/PEEL at 400 nm decreases as the thickness of the optical spacer increases. A sample with four layers of NiO_x optical spacer shows a transmission nearly identical to a sample without PEEL. Given the insights from Fig. 2 and Supplementary Fig. 5, PIRET between AgNWs and BCzBN is contingent upon their distance. Therefore, the rise in transmission of AgNWs/PEEL is primarily driven by PIRET. Furthermore, calculation results point to n_{medium} as the determinant of optical extinction for AgNWs. To rule out its impact on LSPR excitation, the refractive index (n) of PEEL was measured. Figure 4d suggests that BCzBN doping has little influence on the refractive index of NiO_x, albeit causing a slight rise in the extinction coefficient (k) due to the absorption and scattering of BCzBN aggregates. As the simulated absorption spectra shown in Supplementary Fig. 6, the slight change in refractive index has negligible influence on the excitation of LSPR. Therefore, it can be concluded that the improved transparency of AgNWs/PEEL is owing to the LSPR energy recycling rather than the suppression of LSPR excitation. Notably, the measured transmission of AgNWs/PEEL surpasses that of AgNWs/NiO_x in a broad

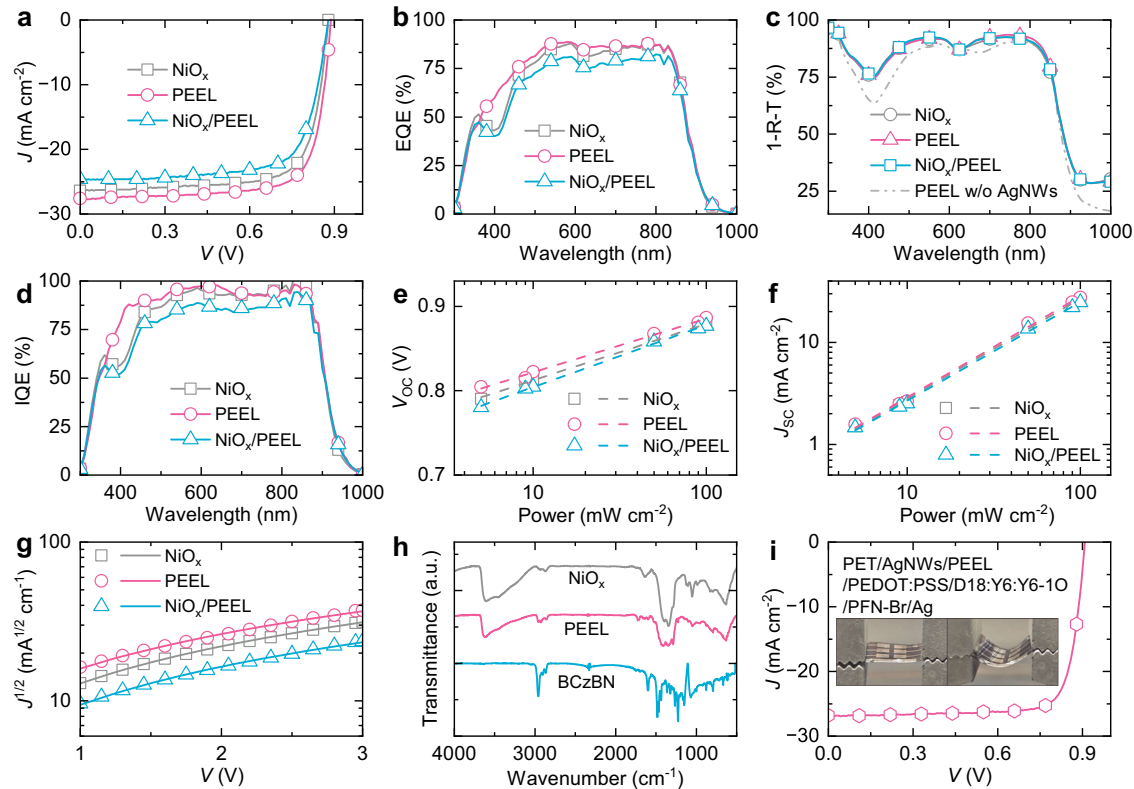


Fig. 5 | Photovoltaic performance of AgNWs-based FOSCs. **a** J - V characteristics, **b** EQE spectra, **c** absorption spectra, and **d** IQE spectra of FOSCs based on NiO_x , PEEL, and NiO_x/PEEL . The absorption spectrum of FOSCs without AgNWs is attached for comparison. A simulated AM 1.5 G light source with a power intensity of 100 mW cm^{-2} was applied. Variation in **e** J_{sc} and **f** V_{oc} of various devices as a

function of incident light intensity. **g** $J^{1/2}$ - V curves for hole-only devices based on various HTLs. **h** FITR spectra of NiO_x , PEEL, and BCzBN. **i** J - V curve of optimized FOSCs based on D18:Y6:Y6-10. Inset shows photographs of flat and bent FOSCs. Source data are provided as a Source Data file.

spectral region, possibly due to PIRET-induced emission and spontaneous emission from BCzBN. To account for potential light scattering from uneven surfaces, the surface morphology of various FTEs was examined using scanning electron microscopy (SEM). The AgNWs were largely encapsulated by NiO_x , reducing the junction height of the nanowires. In the optimized FTEs with two layers of NiO_x or PEEL, the surface appeared nearly level (Fig. 4f–g). However, due to the poor dispersion of NiO_x nanoparticles in tetrahydrofuran, particle aggregation led to pinhole formation. Transmission and haze spectra of three-layered NiO_x (Supplementary Fig. 7) suggest that NiO_x itself contributes minimally to light scattering. Thus, the haze observed in AgNWs/PEEL is attributed to BCzBN emission, highlighting an effective plasmon energy recycling mechanism.

The thickness of PEEL was optimized by varying the number of spin-coating (Supplementary Fig. 8). Compared to single-layer PEEL, two-layer PEEL increases the transmittance of FTE, especially in the

blue region, due to the promoted PIRET. Further increase in PEEL thickness leads to broadband parasitic absorption, which is related to the defect state-mediated absorption of NiO_x NP⁴⁸. The obvious transmittance reduction around 400–500 nm is ascribed to the absorption of BCzBN (Fig. 2a). The optimal thickness of the PEEL was determined to be approximately 80 nm using ellipsometry. To investigate the correlation between AgNWs thickness and plasmonic energy recycling efficiency, we measured transmission spectra of NiO_x and PEEL films with different layers of AgNWs. Quartz substrates were employed to eliminate parasitic optical absorption. Supplementary Fig. 9 confirms enhanced plasmonic losses in thicker AgNWs. Notably, BCzBN incorporation enhanced the optical transparency of AgNWs/ NiO_x across all layer configurations, yet the gradually increased LSPR signals indicate compromised plasmon recycling efficiency. The PEEL film is unable to fully cover the stacked AgNWs and hardly extracts LSPR from the topmost AgNWs according to the distance-dependent feature of FIRET demonstrated in Fig. 4.

Table 1 | Photovoltaic parameters for FOSCs under 100 mW cm^{-2} AM 1.5 G illumination

Active layer	HTLs	V_{oc} (V)	J_{sc} (mA cm^{-2})	FF (%)	PCE (%)	PCE _{ave} (%)
D18:Y6:Y6-10	NiO_x	0.879	26.44	74.09	17.22	17.05
	PEEL	0.887	27.68	75.35	18.50	18.24
	NiO_x/PEEL	0.877	24.63	72.96	15.76	15.51
D18:L8-BO	PEEL	0.908	26.78	80.17	19.51	19.26
	PEEL (certified)	0.907	26.05	79.10	18.69	/

The average PCE (PCE_{ave}) for each FOSC is the statistics of 6 devices.

Device performance of FOSCs

FOSCs with a device structure of PET/AgNWs/ NiO_x or PEEL/PEDOT:PSS/D18:Y6:Y6-10/PDINO/Ag were fabricated to explore the role of plasmon energy recycling in the device performance enhancement. A thin PEDOT:PSS film was spin-coated on NiO_x to flatten the surface, promote the uniform coating of the active layer, and facilitate hole extraction. A moth-eye-based anti-reflective structure was attached to the substrate to enhance light harvesting. Displayed in Fig. 5a are the current density-voltage (J - V) curves of FOSCs, characterized under conditions of simulated AM 1.5 G illumination (100 mW cm^{-2}), air atmosphere, and room temperature. Corresponding derived characteristics are summarized in Table 1. A significant increment was

observed in the short-circuit current density (J_{SC}), from 26.44 mA cm⁻² to 27.68 mA cm⁻², upon BCzBN-doping. Due to the similarity between the valence band of NiO_x and the highest occupied molecular orbital of BCzBN, hole extraction remains relatively unaffected, resulting in a fill factor (FF) of about 75%. Moreover, all devices maintained a constant open circuit voltage (V_{OC}) of 0.887 V. Consequently, the power conversion efficiency (PCE) of FOSCs rose from 17.22% to 18.50% in the presence of PEEL. Notably, inserting an additional optical spacer eliminated any improvement in J_{SC} and decreased FF. The high resistance of the thick NiO_x layer is responsible for the device's performance decay. As a result, FOSCs featuring both PEEL and optical spacer obtained a relatively lower PCE of 15.76%, further illustrating the remarkable impact of plasmon-exciton energy exchange on device performance. To affirm the variations in J_{SC} , external quantum efficiency (EQE) was also characterized. Integrated J_{SC} values derived from the EQE spectra of reference, PEEL-based, and NiO_x/PEEL-based FOSCs are 25.81, 26.75, and 24.03 mA cm⁻², respectively, all in agreement with the measured results (Fig. 5b). The EQE spectra also reveal that BCzBN-doping triggers a broadband increase in EQE with a significant enhancement in the LSPR spectral region. This indicates a significant reduction in the parasitic absorption of AgNWs after applying PEEL, which then effectively transfers plasmon energy to green light emission. Given the low optical out-coupling efficiency typically associated with emission from thin-film devices, it can be inferred that most of the emitted green light is trapped within the device, thereby contributing to the photocurrent of FOSCs. The detailed photovoltaic parameters statistics for 18 devices are shown in Supplementary Fig. 10. The general enhancement of photovoltaic properties after doping BCzBN in the NiO_x layer demonstrates the effectiveness of PIRET. Notably, the AgNW networks were processed with hot-pressing to reduce the junction height according to related reports⁴⁷. A large variation in device performance indicates the poor reproducibility of FOSCs based on pristine AgNWs FTE (Supplementary Fig. 11). In contrast, the devices processed with hot-pressing have a largely improved reproducibility.

Absorption (1-R-T) spectra were also measured to explore the influence of light-harvesting on J_{SC} (Fig. 5c). The results confirm that the absorption of FOSCs is barely affected by introducing a small amount of BCzBN. In addition, FOSCs without AgNWs exhibit a lower absorption at the LSPR region, suggesting considerable parasitic absorption in AgNWs-based FOSCs. The absorption spectra of FOSCs without rear electrodes confirm that the optical loss primarily originates from the localized surface plasmon resonance (LSPR) of AgNWs (Supplementary Fig. 12a). Notably, this optical loss is likely underestimated due to the strong light extinction of the active layer. To more accurately assess optical losses, we calculated those in bare FTEs based on their transmission spectra (Supplementary Fig. 12b). The peak optical loss of the FTE at 400 nm is reduced by 11.9% in the presence of BCzBN, highlighting its role in mitigating plasmonic losses. Under AM1.5G illumination with a power intensity of 73 mW cm⁻² (300–1000 nm), the parasitic absorption of AgNWs results in an energy loss of 3.6 mW cm⁻², whereas the constructed plasmon energy recycling reduces this loss to 1.7 mW cm⁻². Given that the reference device exhibits an integrated J_{SC} of 25.81 mA cm⁻², it can be inferred that plasmon energy recycling alone enhances the photocurrent of FOSCs to 26.64 mA cm⁻², corresponding to a 3.2% increase in PCE. Furthermore, when compared to the 3.6% increase in measured J_{SC} , the relatively lower enhancement in calculated J_{SC} suggests that improved charge extraction also contributes to the observed photocurrent enhancement. To fully investigate the parasitic absorption of AgNWs in integrated devices, FDTD simulations were also performed (Supplementary Fig. 13). The results yield that the simulated optical loss caused by AgNWs is 50.9% and 20.5% at 393 nm and 480 nm, respectively. These results are consistent with the measured transmission spectra of AgNWs in Fig. 4a. The internal quantum efficiency (IQE) spectra displayed in Fig. 5d imply that the photocurrent enhancement

is predominantly driven by an increase in charge generation, particularly notable in the LSPR spectral region. It is concluded that the enhanced photocurrent is primarily due to the boosted generation of charge carriers, signifying a decrease in parasitic absorption within FOSCs. With the adjacent medium changing from air to NiO_x, the LSPR excited on AgNWs undergoes a spectral shift from the ultraviolet to the blue region, resulting in the lowest transmittance. Simultaneously, the high Q_{sca} LSPR in the blue region leads to a relatively higher haze in AgNWs/NiO_x. Since NiO_x serves as the surrounding medium in both AgNWs/NiO_x and AgNWs/NiO_x/PEEL structures, the excitation conditions of LSPR remain unchanged. Due to the spatial isolation effect of the thick NiO_x film (Supplementary Fig. 4), plasmonic energy extraction is largely suppressed, leading to a negligible difference in the optical spectra. Consequently, the EQE response of PEEL- and NiO_x/PEEL-based FOSCs should, in principle, be identical if charge extraction effects are not considered. However, in practice, the increased resistance of the thick NiO_x film impedes hole extraction, resulting in a relatively lower IQE and EQE of NiO_x/PEEL-based devices (Fig. 5b,d).

To elucidate the impact of PEEL on carrier dynamics in FOSCs, we systematically analyzed the light intensity dependence of V_{OC} and J_{SC} . As shown in Fig. 5e, the PEEL-based device exhibits the smallest V_{OC} slope ($1.07 K_B T/q$) compared to counterparts based on NiO_x ($1.12 K_B T/q$) and NiO_x/PEEL ($1.24 K_B T/q$), indicating suppressed monomolecular recombination. The J_{SC} power-law exponents further corroborate this trend, with values of 0.982 (NiO_x), 0.989 (PEEL), and 0.968 (NiO_x/PEEL). The relatively higher exponent for PEEL highlights its superior bimolecular recombination suppression, consistent with enhanced charge extraction balance. Ultraviolet photoelectron spectroscopy (UPS) reveals minimal perturbation to the NiO_x valence band maximum after BCzBN doping (Supplementary Fig. 14), ruling out energy level misalignment as the origin of improved hole extraction. Instead, space-charge-limited current (SCLC) measurements (Fig. 5g) of glass/ITO/HTLs/D18:Y6:IO/MoO_x/Ag demonstrate that BCzBN doping increases the hole mobility of PEEL ($4.44 \times 10^{-3} \text{ cm}^2 \text{ V}^{-1} \text{ s}^{-1}$) by 41% compared to pristine NiO_x ($3.14 \times 10^{-3} \text{ cm}^2 \text{ V}^{-1} \text{ s}^{-1}$), while the NiO_x/PEEL bilayer exhibits reduced mobility ($2.60 \times 10^{-3} \text{ cm}^2 \text{ V}^{-1} \text{ s}^{-1}$) due to interfacial resistance. Fourier-transform infrared spectroscopy (FTIR) directly links these improvements to BCzBN's defect-passivating function (Fig. 5h). The PEEL spectrum shows a 30% reduction in hydroxyl adsorption intensity (3400 cm^{-1}) with a 10 cm^{-1} blue shift, signifying weakened hydrogen bonding. Concurrently, defect-associated peaks at 1050 cm^{-1} and 1636 cm^{-1} decrease by 50% and 90%, respectively, while emergent C-H stretching modes ($2850\text{--}2950 \text{ cm}^{-1}$) confirm BCzBN anchoring. These results establish a mechanistic framework where BCzBN simultaneously passivates oxygen vacancies via electron transfer and enhances hole mobility through interfacial energy landscape modulation. This mobility enhancement aligns with the reduced surface free energy (SFE) of PEEL (37.87 mN m^{-1}) versus NiO_x (71.45 mN m^{-1}), as quantified by the Owens-Wendt-Rabel-Kaelble (OWRK) method (Supplementary Fig. 15 and Supplementary Table 1). The lower SFE arises from tert-butyl-mediated electron donation into oxygen vacancies, passivating dangling bonds, and optimizing interfacial charge transport. It can be concluded that the BCzBN boosted the hole extraction of HTLs, thereby increasing the FF of FOSCs.

The light stability of FOSCs was studied by recording the PCE of FOSCs under AM1.5G (100 mW cm^{-2}) illumination (Supplementary Fig. 16). After 180 min of illumination, the PCEs of NiO_x- and PEEL-based FOSCs were decreased to 94.7% and 96.7% of their initial values, respectively. The slightly improved light stability may originate from the UV-blocking ability of PEEL as revealed by Fig. 2a. BCzBN doping reduces the number of high-energy photons reaching the active layer and prevents degradation of the organic semiconductors. The flexibility of FOSCs was evaluated by monitoring the PCE under repetitive bending cycles with a radius of 5 mm (Supplementary Fig. 17a). Both NiO_x- and PEEL-based devices retained approximately 84% of their initial PCE after 2000 bending cycles, demonstrating that the

incorporation of BCzBN imposes minimal impact on the mechanical flexibility of FOSCs. This conclusion is further corroborated by the invariant optical transmission spectra of AgNWs with and without BCzBN doping (Supplementary Fig. 17b). Notably, while a marginal increase in sheet resistance was observed for both AgNW/NiO_x and AgNW/PEEL electrodes after bending, their values remained statistically indistinguishable (Supplementary Fig. 17c). To demonstrate the universality of PEEL in recycling plasmonic energy, FOSCs with device structure of PET/AgNWs/PEEL/PEDOT:PSS/D18:L8-BO/PFN-Br/Ag were also fabricated and characterized (Fig. 5i). The optimized device obtained a V_{OC} of 0.908 V, J_{SC} of 26.78 mA cm⁻², and FF of 80.17%, yielding a state-of-art efficiency of 19.51%. An FOSC was encapsulated by a PET film and sent to the National Center of Supervision & Inspection on Solar Photovoltaic Products Quality of China (CPVT) for characterization. The certified V_{OC} of 0.907 V, J_{SC} of 26.05 mA cm⁻², and FF of 79.10% generate a PCE of 18.69% (Supplementary Fig. 18). In comparison, the relatively lower efficiency mainly arises from the relatively smaller FF. The performance decay is owing to the poor encapsulating ability of PET.

Discussion

Overall, the plasmon energy loss is mitigated by harnessing the plasmon-exciton energy exchange between AgNWs and emitters. Mie theory calculation and FDTD simulation predominantly point towards the excitation of LSPR as the major contributor to the parasitic absorption of FOSCs. BCzBN with absorption overlaps and emission beyond the excitation of LSPR can act as a coupler that transfers plasmon to radiation. The simultaneously suppressed backward energy and charge transfer benefit the outcoupling of LSPR. Due to the high quantum efficiency of BCzBN, LSPR energy is largely converted to radiation and then absorbed by the active layer, contributing to the photocurrent. The J_{SC} enhancement yields FOSCs with a state-of-the-art PCE of 19.51% and a certified PCE of 18.69%.

In conclusion, efficient plasmon energy recycling is realized by rational design of the spatial position, energy level structure, and spectral overlap between AgNWs, hole transport layer, and emitter. This work demonstrates a candidate configuration for manipulating PIET of surface plasmons and provides a feasible way to reduce the parasitic absorption of FOSCs. More efficient plasmon energy recycling could be obtained by finely controlling spatial distribution, radiation rate, and Stokes shift of emitters, as well as the electric field intensity of surface plasmons.

Methods

Materials

AgNWs solution was purchased from Gu's Material with a diameter of about 30 nm and a length of about 20 μm. NiO_x NP and tetrahydrofuran (≥99.9%) were sourced from Advanced Election Technology and Aladdin, respectively. PEDOT:PSS (Clevios AI 4083) was supplied by Heraeus. Y6 and Y6-IO were procured from eFlex PV, and D18 and L8-BO were acquired from HYPER. PFN-Br was obtained from Solarmer Materials. Chloroform (99.8%) was supplied by Adams. Diiodo benzene was acquired from Sigma Aldrich. PDINO (98%) and carbon disulfide (99%) were obtained from J&K. All chemicals were used as received without further purification.

Device fabrication

For the preparation of the flexible electrode, the solution of AgNWs was spin-coated onto PET substrates (180 μm) at 2000 rpm for 20 s and baked at 100 °C for 5 min. The process was repeated thrice to improve the quantity of AgNWs. NiO_x solution was prepared by dispersing 10 mg NiO_x NP in 400 μL deionized water and 600 μL tetrahydrofuran. The NiO_x film was fabricated by spin-coating the mixed solution onto AgNWs at 4000 rpm for 20 s and then annealed at 140 °C for 15 min. BCzBN doping was carried out by adding different amounts of BCzBN

into NiO_x NP solution and stirring at room temperature for 1 h. PEDOT:PSS was spin-coated on NiO_x at 4000 rpm for 40 s and then annealed at 100 °C for 10 min. Donor solution (5 mg mL⁻¹ of D18 in chloroform) and acceptor solution (8 mg mL⁻¹ of Y6:Y6-IO (0.7:0.3) in chloroform) were subsequently spin-coated on PEDOT:PSS layer at 2000 rpm for 40 s and at 2500 rpm for 40 s, respectively. The prepared active layer was then vapor-assisted annealed in a carbon disulfide atmosphere for 1 min. PDINO was dissolved in methanol with a concentration of 1 mg/mL and spin-coated on the active layer at 2500 rpm for 40 s. As for the D18:L8-BO system, the active layer solution was prepared by dissolving D18 and L8-BO with a weight ratio of 1:1 in diiodo benzene-doped chloroform (5 mg mL⁻¹) at a total concentration of 9 mg mL⁻¹. The mixed solution was stirred at 80 °C for 3 h and then was deposited on the PEDOT:PSS layer at 2000 rpm for 40 s with a thermal annealing process for 10 min in a nitrogen-filled glovebox. PFN-Br was dissolved in methanol with a concentration of 0.5 mg/mL and spin-coated on the active layer at 3000 rpm for 40 s. Eventually, a 200 nm Ag film was deposited through thermal evaporation at a pressure of 6×10^{-4} Torr. The effective area of the devices was determined to be 0.0625 cm² by employing a shadow mask with aperture area measured using contour measuring machines.

Film and device characterizations

The surface morphologies were measured by SEM (SU8230). Transmittance, absorption, and reflection spectra were measured using an ultraviolet-visible-near infrared spectrometer (Perkin Elmer Lambda 1050+) with an integrating sphere. Steady-state photoluminescence (PL) spectra were recorded on an FM-4 type fluorescence spectrophotometer (JY company, French). A confocal Raman imaging system (WiTec Alpha300R) was employed to obtain the PL mapping results. Transient absorption measurements were carried out on a Helios pump-probe system (Ultrafast Systems LLC) combined with an amplified femtosecond laser system (Coherent). FTIR spectra were measured by Bruke VERTEX 70. The J - V characteristics of flexible devices were measured by Keithley 2612 source meter under simulated AM 1.5 G solar irradiation at 100 mW cm⁻² which was produced by Oriel model 91160. The EQE spectra were measured by a photo-modulation spectroscopic setup (Enli Technology Co. Ltd., QE-R).

Reporting summary

Further information on research design is available in the Nature Portfolio Reporting Summary linked to this article.

Data availability

Source data are provided with this paper.

References

- Campos, A. et al. Plasmonic quantum size effects in silver nanoparticles are dominated by interfaces and local environments. *Nat. Phys.* **15**, 275–280 (2019).
- Kravets, V. G., Kabashin, A. V., Barnes, W. L. & Grigorenko, A. N. Plasmonic Surface Lattice Resonances: A Review of Properties and Applications. *Chem. Rev.* **118**, 5912–5951 (2018).
- Lalanne, P., Yan, W., Vynck, K., Sauvan, C. & Hugonin, J. P. Light Interaction with Photonic and Plasmonic Resonances. *Laser Photonics Rev.* **12**, 1700113 (2018).
- Gao, D. et al. Optical manipulation from the microscale to the nanoscale: fundamentals, advances and prospects. *Light Sci. Appl.* **6**, e17039 (2017).
- Jang, Y. H. et al. Plasmonic Solar Cells: From Rational Design to Mechanism Overview. *Chem. Rev.* **116**, 14982–15034 (2016).
- Chen, J.-D. et al. Polymer Solar Cells with 90% External Quantum Efficiency Featuring an Ideal Light- and Charge-Manipulation Layer. *Adv. Mater.* **30**, 1706083 (2018).

7. Kazuma, E. & Kim, Y. Mechanistic Studies of Plasmon Chemistry on Metal Catalysts. *Angew. Chem. Int. Ed.* **58**, 4800–4808 (2019).
8. Li, J. et al. Plasmon-induced resonance energy transfer for solar energy conversion. *Nat. Photon.* **9**, 601–607 (2015).
9. Liu, D. & Xue, C. Plasmonic Coupling Architectures for Enhanced Photocatalysis. *Adv. Mater.* **33**, 2005738 (2021).
10. Boriskina, S. V. et al. Losses in Plasmonics: from Mitigating Energy Dissipation to Embracing Loss-Enabled Functionalities. *Adv. Opt. Photonics* **9**, 775 (2017).
11. Chen, J.-D. et al. Hot-electron emission-driven energy recycling in transparent plasmonic electrode for organic solar cells. *InfoMat* **4**, e12285 (2022).
12. Zhang, N., Han, C., Fu, X. & Xu, Y.-J. Function-Oriented Engineering of Metal-Based Nanohybrids for Photoredox Catalysis: Exerting Plasmonic Effect and Beyond. *Chem* **4**, 1832–1861 (2018).
13. West, P. R. et al. Searching for better plasmonic materials. *Laser Photonics Rev.* **4**, 795–808 (2010).
14. Derkachova, A., Kolwas, K. & Demchenko, I. Dielectric Function for Gold in Plasmonics Applications: Size Dependence of Plasmon Resonance Frequencies and Damping Rates for Nanospheres. *Plasmonics* **11**, 941–951 (2015).
15. Zhang, Z., Zhang, C., Zheng, H. & Xu, H. Plasmon-Driven Catalysis on Molecules and Nanomaterials. *Acc. Chem. Res.* **52**, 2506–2515 (2019).
16. Wu, B. et al. Uncovering Loss Mechanisms in Silver Nanoparticle-Blended Plasmonic Organic Solar Cells. *Nat. Commun.* **4**, 2004 (2013).
17. Chen, J.-D. et al. Single-Junction Polymer Solar Cells Exceeding 10% Power Conversion Efficiency. *Adv. Mater.* **27**, 1035–1041 (2014).
18. Haffner, C. et al. Low-loss plasmon-assisted electro-optic modulator. *Nature* **556**, 483–486 (2018).
19. Khurgin, J. B. How to deal with the loss in plasmonics and meta-materials. *Nat. Nanotech.* **10**, 2–6 (2015).
20. Li, W. & Valentine, J. G. Harvesting the loss: surface plasmon-based hot electron photodetection. *Nanophotonics* **6**, 177–191 (2017).
21. Xiong, X. et al. Silver nanowires for photonics applications. *Laser Photonics Rev.* **7**, 901–919 (2013).
22. Huang, S., Liu, Y., Zhao, Y., Ren, Z. & Guo, C. F. Flexible Electronics: Stretchable Electrodes and Their Future. *Adv. Funct. Mater.* **29**, 1805924 (2018).
23. Chen, D., Liang, J. & Pei, Q. Flexible and stretchable electrodes for next generation polymer electronics: a review. *Sci. China Chem.* **59**, 659–671 (2016).
24. Azani, M. R., Hassanpour, A. & Torres, T. Benefits, Problems, and Solutions of Silver Nanowire Transparent Conductive Electrodes in Indium Tin Oxide (ITO)-Free Flexible Solar Cells. *Adv. Energy Mater.* **10**, 2002536 (2020).
25. Park, J. H. et al. Flash-Induced Self-Limited Plasmonic Welding of Silver Nanowire Network for Transparent Flexible Energy Harvester. *Chem. Rev.* **29**, 1603473 (2016).
26. Zeng, G. et al. Realizing 17.5% Efficiency Flexible Organic Solar Cells via Atomic-Level Chemical Welding of Silver Nanowire Electrodes. *J. Am. Chem. Soc.* **144**, 8658–8668 (2022).
27. Sun, Y. et al. Flexible organic photovoltaics based on water-processed silver nanowire electrodes. *Nat. Electron.* **2**, 513–520 (2019).
28. Chen, Z. et al. Small-molecular donor guest achieves rigid 18.5% and flexible 15.9% efficiency organic photovoltaic via fine-tuning microstructure morphology. *Joule* **5**, 2395–2407 (2021).
29. Ge, Y. et al. Direct Room Temperature Welding and Chemical Protection of Silver Nanowire Thin Films for High Performance Transparent Conductors. *J. Am. Chem. Soc.* **140**, 193–199 (2017).
30. Li, Y., Xu, G., Cui, C. & Li, Y. Flexible and Semitransparent Organic Solar Cells. *Adv. Energy Mater.* **8**, 1701791 (2017).
31. Meng, X. et al. A General Approach for Lab-to-Manufacturing Translation on Flexible Organic Solar Cells. *Adv. Mater.* **4**, 1903649 (2019).
32. Ren, H. et al. Unraveling the electrical energy loss in silver nanowire electrodes for flexible and Large-Area organic solar cells. *Chem. Eng. J.* **481**, 148498 (2024).
33. Ren, H. et al. 20.4% Power conversion efficiency from albedo-collecting organic solar cells under 0.2 albedo. *Sci. Adv.* **10**, eadp9439 (2024).
34. Kim, K., Yoon, S. J. & Kim, D. Nanowire-based enhancement of localized surface plasmon resonance for highly sensitive detection: a theoretical study. *Opt. Express* **14**, 12419 (2006).
35. Garnett, E. C. et al. Self-limited plasmonic welding of silver nanowire junctions. *Nanophotonics* **11**, 241–249 (2012).
36. Kottmann, J. P., Martin, O. J. F., Smith, D. R. & Schultz, S. Plasmon resonances of silver nanowires with a nonregular cross section. *Phys. Rev. B* **64**, 235402 (2001).
37. Alzoubi, F. Y. et al. Localize surface plasmon resonance of silver nanoparticles using Mie theory. *J. mater. Sci. -mater. El.* **34**, 2128 (2023).
38. Hwang, J. et al. Influence of polyvinylpyrrolidone (PVP) capping layer on silver nanowire networks: theoretical and experimental studies. *RSC Adv.* **6**, 30972–30977 (2016).
39. Ge, Y. et al. Rapid Electrochemical Cleaning Silver Nanowire Thin Films for High-Performance Transparent Conductors. *J. Am. Chem. Soc.* **141**, 12251–12257 (2019).
40. Fang, Y. & Tian, X. Resonant surface plasmons of a metal nanosphere treated as propagating surface plasmons. *Chin. Phys. B* **27**, 067302 (2018).
41. Choi, Y. M. et al. Retarded Charge–Carrier Recombination in Photoelectrochemical Cells from Plasmon-Induced Resonance Energy Transfer. *Adv. Energy Mater.* **10**, 2000570 (2020).
42. Hsu, L.-Y., Ding, W. & Schatz, G. C. Plasmon-Coupled Resonance Energy Transfer. *J. Phys. Chem. Lett.* **8**, 2357–2367 (2017).
43. Shan, H. et al. Direct observation of ultrafast plasmonic hot electron transfer in the strong coupling regime. *Light Sci. Appl.* **8**, 9 (2019).
44. Tagliabue, G. et al. Ultrafast hot-hole injection modifies hot-electron dynamics in Au/p-GaN heterostructures. *Nat. Mater.* **19**, 1312–1318 (2020).
45. Xu, S. et al. Solution-processed multi-resonance organic light-emitting diodes with high efficiency and narrowband emission. *Chin. Chem. Lett.* **32**, 1372–1376 (2021).
46. Dimitriev, O. P. et al. Excimer Emission in J-Aggregates. *J. Phys. Chem. Lett.* **9**, 2138–2214 (2018).
47. Li, W. et al. Recent Progress in Silver Nanowire Networks for Flexible Organic Electronics. *J. Mater. Chem. C* **8**, 4636–4674 (2020).
48. Ma, F. et al. Nickel Oxide for Inverted Structure Perovskite Solar Cells. *J. Energy Chem.* **52**, 393–411 (2021).
49. Zhang, Y. et al. Synergetic Transparent Electrode Architecture for Efficient Non-Fullerene Flexible Organic Solar Cells with >12% Efficiency. *ACS Nano* **13**, 4686–4694 (2019).

Acknowledgements

The authors acknowledge the financial support from the National Natural Science Foundation of China (Nos. U23A20371, T2425024, 62274117, 62275181, 52303244), the Science and Technology Development Fund (FDCT), Macau (No. 0009/2022/AGJ), the Bureau of Science and Technology of Suzhou Municipality (No. SYC2022144), the Macao Youth Scholars Program (No. AM2022008), and Collaborative Innovation Center of Suzhou Nano Science & Technology.

Author contributions

J.C, H.R., F.X, and J.Z contributed equally to this work. J.C., Y.L., and J.T. conceived the idea for the study and designed the experiments. H.R. fabricated the devices and characterized the device performance. F.X.

and H.L. prepared the organic emitter. J.Z. performed the film characterizations. A.S.I. assisted in flexible electrode fabrication. Y.Z. carried out FTIR measurements. J.C. and H.R. analyzed the data and wrote the manuscript. Y.L. and J.T. edited the manuscript. All authors contributed to the manuscript.

Competing interests

The authors declare no competing interests.

Additional information

Supplementary information The online version contains supplementary material available at <https://doi.org/10.1038/s41467-025-59286-0>.

Correspondence and requests for materials should be addressed to Yan-Qing Li or Jian-Xin Tang.

Peer review information *Nature Communications* thanks the anonymous, reviewer(s) for their contribution to the peer review of this work. A peer review file is available.

Reprints and permissions information is available at <http://www.nature.com/reprints>

Publisher's note Springer Nature remains neutral with regard to jurisdictional claims in published maps and institutional affiliations.

Open Access This article is licensed under a Creative Commons Attribution-NonCommercial-NoDerivatives 4.0 International License, which permits any non-commercial use, sharing, distribution and reproduction in any medium or format, as long as you give appropriate credit to the original author(s) and the source, provide a link to the Creative Commons licence, and indicate if you modified the licensed material. You do not have permission under this licence to share adapted material derived from this article or parts of it. The images or other third party material in this article are included in the article's Creative Commons licence, unless indicated otherwise in a credit line to the material. If material is not included in the article's Creative Commons licence and your intended use is not permitted by statutory regulation or exceeds the permitted use, you will need to obtain permission directly from the copyright holder. To view a copy of this licence, visit <http://creativecommons.org/licenses/by-nc-nd/4.0/>.

© The Author(s) 2025